Applied Mathematical Modelling 147 (2025) 116206

Contents lists available at ScienceDirect

Applied Mathematical Modelling

journal homepage: www.elsevier.com/locate/apm

Saffman-Taylor fingering instabilities in shear-thinning fluids displacing Newtonian fluids

A.J. Hutchinson [a,b,*]

[a] Department of Mathematics, Manchester Centre for Nonlinear Dynamics, University of Manchester, Oxford Road, Manchester, M13 9PL, United Kingdom

[b] Department of Computer Science and Applied Mathematics, University of the Witwatersrand, Johannesburg, Jan Smuts Avenue, Johannesburg, 2050, South Africa

ARTICLE INFO

Keywords:
Saffman-Taylor instability
Viscous fingering
Hele-Shaw cell
Shear-thinning fluids
Oil recovery

ABSTRACT

We investigate the radial injection of a shear-thinning fluid, initially occupying a disk of a given radius, into the narrow gap between two parallel plates, displacing a viscous Newtonian fluid. In the Newtonian analogue, the Saffman-Taylor fingering instability occurs when a more viscous fluid is displaced by a less viscous one. Further complications arise when the displacing fluid is shear-thinning because its viscosity increases with radial distance from the source. A linear stability analysis, in which sinusoidal perturbations to the interface between the two fluids are considered, shows that each disturbance, characterised by a mode number, has a corresponding radius that governs the stability of that mode. These radii increase with mode number, approaching a critical radius. If the radius of the initial disk is greater than this critical radius, all modes are stable and the fingering instability is suppressed. This critical radius depends on the ratio of the viscosity of the displaced Newtonian fluid and another viscosity corresponding to the shear-thinning fluid, which we will refer to as the effective viscosity. The theoretical results are contrasted with observations from laboratory experiments. Significant discrepancies between theory and experiment suggest that the underlying physics governing stability is not yet fully understood. We consider various improvements to the model, and by once again comparing theory and experiment, we show that surface tension does not appear to play a pivotal role, but that wall-slip potentially leads to substantial changes in the theoretical predictions.

1. Introduction

When a less viscous fluid invades a more viscous one in a narrow gap between two boundaries or within a porous medium, the interface between the two fluids can become unstable, and any protrusions of the less viscous fluid into the more viscous one can develop into extended fingers. The mechanism behind the development of these fingers is due to the driving pressure gradient having a greater magnitude in the more viscous displaced fluid than in the less viscous intruding one. As a result, any protrusion of the more mobile, less viscous fluid into the higher-viscosity, less mobile ambient, which has a greater driving pressure gradient, will advance further than the surrounding ambient fluid, forming an extended finger. In each fluid, the pressure gradients depend on

* Correspondence to: Department of Mathematics, Manchester Centre for Nonlinear Dynamics, University of Manchester, Oxford Road, Manchester, M13 9PL, United Kingdom.

E-mail address: Ashleigh.Hutchinson@Manchester.ac.uk.

https://doi.org/10.1016/j.apm.2025.116206
Received 20 February 2025; Received in revised form 12 May 2025; Accepted 19 May 2025

Available online 26 May 2025

viscous transverse stresses, typical of shear-dominated flows. Although this phenomenon, commonly referred to as the Saffman-Taylor instability [1], dates back to the late 1950s, it remains of fundamental interest and continues to be relevant in areas such as enhanced oil recovery [2].

Earlier studies on Saffman-Taylor instabilities have been undertaken for Newtonian fluids in two-dimensional [3,4] and axisymmetric geometries [5,6]. However, they are also known to occur in non-Newtonian fluids, and have been observed in more recent Hele-Shaw cell experiments where a less viscous Newtonian fluid intrudes into either a yield-stress fluid [7–9] or a shear-thinning fluid [10–12] within a narrow gap.

Theoretical treatments of such systems often involve using a modified version of Darcy's law to describe the non-Newtonian flow (see [13] for example) while neglecting the viscosity of the less viscous, displacing Newtonian fluid. Studies adopting this approach have been undertaken to model the displacement of a non-Newtonian fluid by an inviscid fluid in radial geometries and in 2-D channels [14–16]. Theoretical developments have progressed to the case where the displacing fluid is replaced by another non-Newtonian fluid [17–19]. In general, the non-Newtonian effects modify the fingering pattern by suppressing tip-splitting and creating sideways branches (see [20] for example). An alternative to the modified Darcy's law approach for such systems was provided by Wilson [21], who developed a theoretical model for the displacement of a non-Newtonian fluid by air within a 2-D geometry, using the thin-film equations with the viscosity of the non-Newtonian fluid described using either an Oldroyd or power-law model. The dynamics of the air were neglected, and a linear stability analysis was performed on the thin-film equations and boundary conditions to derive the stability criteria.

Although Saffman-Taylor instabilities have been thoroughly investigated for a variety of flow configurations, in the current paper, we consider a setup that has not been subjected to critical examination. In particular, we adopt a similar approach to that of Wilson [21], but instead, we examine the radial displacement of a viscous Newtonian fluid by a shear-thinning power-law fluid within a Hele-Shaw cell. This is essentially the reverse configuration of the more well-studied case in which a non-Newtonian fluid is displaced by a less viscous Newtonian one. In contrast to the 2-D channel flows explored by Wilson [21], further complications arise in this axisymmetric configuration due to the viscosity of the shear-thinning fluid increasing with radial distance from the source as a result of the fluid velocity decreasing radially. Consequently, the initial injection radius becomes important in determining whether or not Saffman-Taylor instabilities are a feature of these flows at early times. In addition, when fingers do form at early times, as they continue to grow within the ambient fluid, the viscosity of the fingers themselves increases and they become less mobile, suggesting suppression at later stages, and perhaps even a return to axisymmetric flow. Unlike Wilson's model and many others mentioned earlier, we do not neglect the dynamics of the Newtonian fluid and instead impose appropriate conditions at the fluid-fluid interface, allowing for a more complete description of the fluid flow. We also compare the results from some laboratory experiments to the predictions from the mathematical model and propose further improvements to the mathematical model.

The current research will begin with the thin-film equations governing the flow in a Hele-Shaw cell to describe the radial injection of a shear-thinning fluid, which initially starts with a finite injection radius a_0, into a narrow gap containing a viscous Newtonian fluid. Using a linear stability analysis, we derive an expression for the critical radius of injection a_c which is determined by a ratio of viscosities corresponding to the Newtonian fluid and the shear-thinning fluid. Unlike the Newtonian fluid where the viscosity is constant, the viscosity corresponding to the shear-thinning fluid defined in this ratio, which will be referred to as the effective viscosity, depends on radial distance from the source. We find that for $a_0 > a_c$, which corresponds to the case where the effective viscosity of the shear-thinning fluid at the (initial) interface is larger than that of the Newtonian fluid, viscous fingers do not form and the flow remains stable for all time. Our linear stability analysis also shows that each sinusoidal interfacial disturbance of mode number $k = 2, 3\ldots$ has an associated critical radius a_k, where for $a_k < a_0 < a_{k+1}$, all modes $m \leq k$ are stable, while modes $m > k$ are initially unstable. The sequence of critical radii a_k is an increasing function of k and bounded above by a_c.

The next part of this research focuses on laboratory experiments in which a shear-thinning fluid called Xanthan gum is injected radially into the narrow gap between two glass plates, displacing a viscous silicone oil. Parameters such as the input flux, the initial radius of injection a_0, and the viscosity of the silicone oil were varied. We compare the critical radius a_c, derived theoretically, to what we observe experimentally. We will see that there are significant discrepancies between theory and experiment, which we attempt to resolve by adjusting the theoretical model to include surface tension and wall-slip. It is worth noting that laboratory experiments involving the displacement of silicone oil by Xanthan gum within a fracture have been undertaken [22], but in a different setup to the one explored in the current work.

To the best of my knowledge, there has been little direct investigation into the situation described here. Perhaps the closest related research articles are the purely theoretical studies by Pascal [23,24] and Sader et al. [25]. Pascal developed a mathematical model for the radial displacement of either a non-Newtonian [24] or Newtonian fluid [23] by an intruding non-Newtonian fluid within a porous medium. A modified Darcy's law was used to describe the non-Newtonian flow behaviour, and interfacial surface tension was neglected. Hele-Shaw flows are analogous to porous media flows, so we expect the stability criteria deduced by Pascal to also apply to Hele-Shaw flows. Although our approach to modelling the flow in a Hele-Shaw cell differs in that we use the thin-film equations as opposed to a modified Darcy's law, as well as incorporating surface tension at a later stage, we will see that the stability criteria are consistent when surface tension is considered negligible. Sader et al. [25] investigated the intrusion of an inviscid fluid into a non-Newtonian power-law fluid in a radial Hele-Shaw cell, where the dynamics of the inviscid fluid were neglected. If the dynamics of the displacing fluid were retained and the viscosity non-zero, this would be the reverse configuration of the problem addressed in the current work. The linear stability analysis predicted the existence of a critical injection radius below which the flow would always be stable. As a consequence of neglecting the dynamics of the displacing fluid, this critical radius depended only on the surface tension at the fluid-fluid interface and not on the viscosity ratio - an important feature of the Hele-Shaw flows we investigate.

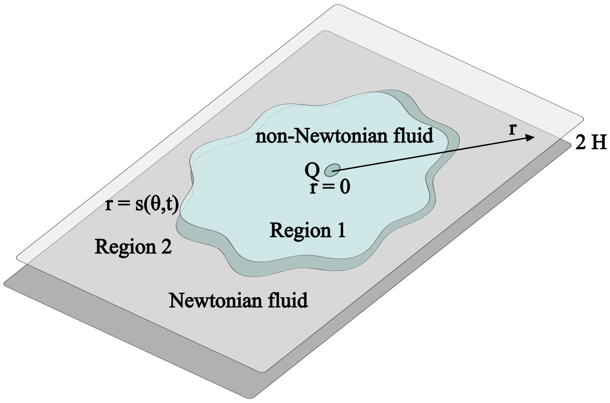

Fig. 1. Displacement of a high-viscosity Newtonian fluid in a narrow gap of size $2H$ by a shear-thinning fluid released from a point source at a constant flux Q. Polar coordinates (r, θ, z) are used with the injection point located at $r = 0$. The shear-thinning fluid and the Newtonian fluid occupy Regions 1 and 2 respectively, where $r = s(\theta, t)$ is the interface between the two fluids.

This paper is presented as follows. In Section 2, the theoretical model which consists of the governing equations in each of the two fluids, as well as the interface conditions, is derived. A linear stability analysis is performed, and the critical radius of injection as well as the critical radius for each mode is obtained. In Section 3, the predictions from the theoretical model are compared with experimental observations. In Section 4, various improvements to the theoretical model are considered, and conclusions are given in Section 5.

2. Mathematical model

A shear-thinning fluid is injected from a small circular hole at a constant flux Q into a narrow gap of size $2H$ between two parallel plates. The fluid, which initially occupies a disk of radius a_0 at time $t = 0$, displaces a viscous Newtonian fluid as it spreads radially outward, as shown in Fig. 1. For now, we assume the shear-thinning fluid displaces the Newtonian fluid completely, maintaining contact with the cell walls, where the no-slip condition applies. We will use polar coordinates (r, θ, z) orientated so that the injection point is located at $r = 0$, and the walls of the Hele-Shaw cell are at $z = \pm H$. In this setup, we define Region 1, $0 < r < s(\theta, t)$, as the domain occupied by the shear-thinning fluid, and Region 2, $s(\theta, t) < r < \infty$, as the region filled by the displaced Newtonian fluid, with the fluid-fluid interface located at $r = s(\theta, t)$.

We first consider Region 1, $0 < r < s(\theta, t)$, occupied by the shear-thinning fluid. The velocity in the z direction is negligible. Let the r and θ components of the velocity be denoted by $u(r, \theta, z)$ and $v(r, \theta, z)$ respectively, and the fluid pressure by $p(r, \theta, z)$. Sufficiently far from the source, where $r \gg 2H$, we invoke the thin-film approximation, in which vertical gradients of shear stress are balanced by radial and azimuthal pressure gradients. Along with conservation of mass, the governing equations are

$$\frac{\partial p}{\partial r} = \frac{\partial}{\partial z}\left(\mu(r, \theta, z)\frac{\partial u}{\partial z}\right), \tag{1}$$

$$\frac{1}{r}\frac{\partial p}{\partial \theta} = \frac{\partial}{\partial z}\left(\mu(r, \theta, z)\frac{\partial v}{\partial z}\right), \tag{2}$$

$$\frac{\partial p}{\partial z} = 0, \tag{3}$$

$$\frac{\partial u}{\partial r} + \frac{u}{r} + \frac{1}{r}\frac{\partial v}{\partial \theta} = 0. \tag{4}$$

The viscosity $\mu(r, \theta, z)$ of the shear-thinning fluid is modelled using a power-law of the form

$$\mu(r, \theta, z) = m\left[\frac{1}{2}e_{ij}e_{ij}\right]^{(1-n)/2n}, \tag{5}$$

where n is the power-law index, m is the consistency factor, and e_{ij} is the rate-of-strain tensor. Within the lubrication approximation, the viscosity (5) reduces to

$$\mu(r, \theta, z) = 2^{1-1/n} m\left[\left(\frac{\partial u}{\partial z}\right)^2 + \left(\frac{\partial v}{\partial z}\right)^2\right]^{(1-n)/2n}. \tag{6}$$

Note that $n = 1$ describes Newtonian fluids, and shear-thickening fluids satisfy $0 < n < 1$. We will only be concerned with shear-thinning fluids where $n > 1$.

From (3), p is independent of z and so we can integrate equations (1) and (2) with respect to z. From vertical symmetry of the setup we infer that

$$\frac{\partial u}{\partial z}(r, \theta, 0) = 0, \quad \frac{\partial v}{\partial z}(r, \theta, 0) = 0,$$

and therefore, the constants of integration are zero, resulting in

$$z\frac{\partial p}{\partial r} = 2^{1-1/n} m \left[\left(\frac{\partial u}{\partial z}\right)^2 + \left(\frac{\partial v}{\partial z}\right)^2 \right]^{(1-n)/2n} \frac{\partial u}{\partial z}, \tag{7}$$

$$\frac{z}{r}\frac{\partial p}{\partial \theta} = 2^{1-1/n} m \left[\left(\frac{\partial u}{\partial z}\right)^2 + \left(\frac{\partial v}{\partial z}\right)^2 \right]^{(1-n)/2n} \frac{\partial v}{\partial z}. \tag{8}$$

The boundary conditions at each plate are the no-slip conditions,

$$u(r,\theta,\pm H) = 0, \quad v(r,\theta,\pm H) = 0. \tag{9}$$

In the calculations that follow, we will consider the top half $0 \le z \le H$ only.

2.1. The base flow

Our first task is to derive the base flow solution with velocity $(u_0(r,z),0)$ and pressure $p_0(r)$ by assuming the flow spreads axisymmetrically. The disk occupied by the shear-thinning fluid has time-dependent radius

$$a(t) = \sqrt{a_0^2 + \frac{Qt}{2\pi H}},$$

and mass conservation imposes the constraint

$$\bar{u}_0(r) = \frac{Q}{4\pi H r}, \quad 0 < r \le a(t), \text{ where } \bar{u}_0(r) = \frac{1}{H}\int_0^H u_0(r,z)dz \tag{10}$$

is the depth-averaged radial velocity. Setting $v = 0$ and solving (7) subject to (9) and (10) gives the radial velocity

$$u_0(r,z) = \frac{n+2}{n+1}\frac{Q}{4\pi H r}\left[1 - \left(\frac{z}{H}\right)^{n+1}\right], \tag{11}$$

radial pressure gradient

$$\frac{dp_0}{dr} = -2^{1-1/n} m \left[\frac{(n+2)Q}{4\pi H^{n+2} r}\right]^{1/n}, \tag{12}$$

and viscosity

$$\mu_0(r,z) = m\left[\frac{8\pi H^2 r}{(n+2)Q}\right]^{1-1/n}\left[\frac{H}{z}\right]^{n-1}. \tag{13}$$

From (13) we see that the viscosity is infinite along the centreline $z = 0$, which is a consequence of using a power-law viscosity model with $n > 1$. The minimum viscosity is attained at the walls when $z = H$,

$$\mu_{min}(r) = m\left[\frac{8\pi H^2 r}{(n+2)Q}\right]^{1-1/n}, \tag{14}$$

where the shear is the greatest.

Before introducing a perturbation to the base flow, we define the following dimensionless variables:

$$\begin{aligned} &Z = \frac{z}{H}, \quad R = \frac{r}{a_0}, \quad A = \frac{a}{a_0}, \quad S = \frac{s}{a_0}, \quad T = \frac{t}{4\pi H a_0^2/Q}, \\ &U = \frac{u}{Q/(4\pi H a_0)}, \quad V = \frac{v}{Q/(4\pi H a_0)}, \\ &M = \frac{\mu}{\mu_{min}(a_0)}, \quad P = \frac{p}{Q\mu_{min}(a_0)/(4\pi H^3)}, \end{aligned} \tag{15}$$

where $\mu_{min}(a_0)$, obtained by setting $r = a_0$ in (14), is used to non-dimensionalise the viscosity. In terms of the dimensionless variables (15), the base flow solution given by (11), (12) and (13) is

$$U_0(R,Z) = \frac{n+2}{n+1}\frac{1}{R}\left(1 - Z^{n+1}\right), \quad \frac{dP_0}{dR} = -(n+2)R^{-1/n}, \tag{16}$$

$$M_0(R,Z) = R^{1-1/n} Z^{1-n}, \tag{17}$$

with the interface evolving with T as

$$A(T) = \sqrt{1+2T}.$$

The governing equations (7) and (8) become

$$Z\frac{\partial P}{\partial R} = M\frac{\partial U}{\partial Z}, \quad \frac{Z}{R}\frac{\partial P}{\partial \theta} = M\frac{\partial V}{\partial Z}, \tag{18}$$

where the viscosity in (6) has the dimensionless form

$$M = (n+2)^{1-1/n}\left[\left(\frac{\partial U}{\partial Z}\right)^2 + \left(\frac{\partial V}{\partial Z}\right)^2\right]^{(1-n)/2n}. \tag{19}$$

The continuity equation (4) is invariant under the transformations in (15).

2.2. First-order perturbations

We now consider perturbations to the base flow of the form

$$\begin{aligned}
&S(\theta,T) = A(T) + \zeta(\theta,T),\\
&P(R,\theta,T) = P_0(R) + P_1(R,\theta,T),\\
&U(R,\theta,Z,T) = U_0(R,Z) + U_1(R,\theta,Z,T),\\
&V(R,\theta,Z,T) = V_1(R,\theta,Z,T),\\
&M(R,\theta,Z,T) = M_0(R,Z) + M_1(R,\theta,Z,T).
\end{aligned} \tag{20}$$

Substituting the perturbation expansions for the velocity components U and V in (20) into (19) yields

$$\begin{aligned}
M &= (n+2)^{1-1/n}\left[\left(\frac{\partial U_0}{\partial Z} + \frac{\partial U_1}{\partial Z}\right)^2 + \left(\frac{\partial V_1}{\partial Z}\right)^2\right]^{(1-n)/2n}\\
&= (n+2)^{1-1/n}\left|\frac{\partial U_0}{\partial Z}\right|^{(1-n)/n}\left[1 + 2\left(\frac{\partial U_0}{\partial Z}\right)^{-1}\frac{\partial U_1}{\partial Z} + \ldots\right]^{(1-n)/2n}
\end{aligned}$$

and expanding to first order leads to

$$M \approx (n+2)^{1-1/n}\left|\frac{\partial U_0}{\partial Z}\right|^{(1-n)/n}\left[1 + \frac{1-n}{n}\left(\frac{\partial U_0}{\partial Z}\right)^{-1}\frac{\partial U_1}{\partial Z}\right]. \tag{21}$$

From (16) and (17),

$$M_0 = (n+2)^{1-1/n}\left|\frac{\partial U_0}{\partial Z}\right|^{(1-n)/n},$$

and from (21) we obtain

$$M_1 = \frac{1-n}{n}M_0\left(\frac{\partial U_0}{\partial Z}\right)^{-1}\frac{\partial U_1}{\partial Z}.$$

By noting that

$$M_1\frac{\partial U_0}{\partial Z} = \frac{1-n}{n}M_0\frac{\partial U_1}{\partial Z},$$

substituting the expansions (20) into (18) and the dimensionless form of (4), the zeroth-order equations are identically satisfied, and we obtain the governing equations

$$Z\frac{\partial P_1}{\partial R} = \frac{1}{n}M_0\frac{\partial U_1}{\partial Z}, \quad \frac{Z}{R}\frac{\partial P_1}{\partial \theta} = M_0\frac{\partial V_1}{\partial Z}, \tag{22}$$

$$\frac{\partial U_1}{\partial R} + \frac{U_1}{R} + \frac{1}{R}\frac{\partial V_1}{\partial \theta} = 0, \tag{23}$$

for the perturbations, which must be solved subject to the dimensionless no-slip boundary condition

$$U_1(R,\theta,1,T) = 0, \quad V_1(R,\theta,1,T) = 0. \tag{24}$$

To derive an equation for the pressure P_1, we integrate (22) and use the no-slip condition (24) to obtain U_1 and V_1, from which we can determine the average velocities:

$$\overline{U}_1 = -\frac{n}{n+2}R^{1/n-1}\frac{\partial P_1}{\partial R}, \quad \overline{V}_1 = -\frac{1}{n+2}R^{1/n-2}\frac{\partial P_1}{\partial \theta}. \tag{25}$$

Upon substitution of these averaged quantities into the dimensionless averaged form of the continuity equation in (23), namely,

$$\frac{\partial}{\partial R}(R\overline{U}_1) + \frac{\partial \overline{V}_1}{\partial \theta} = 0,$$

we obtain

$$\frac{\partial}{\partial R}\left(nR^{1/n}\frac{\partial P_1}{\partial R}\right) + R^{1/n-2}\frac{\partial^2 P_1}{\partial \theta^2} = 0. \tag{26}$$

Equation (26) is equivalent to the result derived by Pascal [24] for porous media flows.

We can derive the corresponding expressions for Region 2, $s(\theta,t) < r$, by setting $n = 1$ and by replacing the viscosity with the dimensionless ratio $\mu_N/\mu_{min}(a_0)$. We will use a superscript (N) to denote the variables in Region 2. The dimensionless base flow and first order perturbation average velocities are

$$U_0^{(N)} = \frac{3}{2}\frac{1}{R}\left(1 - Z^2\right), \quad \frac{dP_0^{(N)}}{dR} = -\frac{3\mu_N}{\mu_{min}(a_0)}\frac{1}{R}, \tag{27}$$

$$\overline{U}_1^{(N)} = -\frac{\mu_{min}(a_0)}{3\mu_N}\frac{\partial P_1^{(N)}}{\partial R}, \quad \overline{V}_1^{(N)} = -\frac{\mu_{min}(a_0)}{3\mu_N}\frac{1}{R}\frac{\partial P_1^{(N)}}{\partial \theta}, \tag{28}$$

respectively, and the pressure $P_1^{(N)}$ satisfies the Laplace equation

$$R\frac{\partial}{\partial R}\left(R\frac{\partial P_1^{(N)}}{\partial R}\right) + \frac{\partial^2 P_1^{(N)}}{\partial \theta^2} = 0. \tag{29}$$

2.3. Interface conditions

At the interface between the two fluids, we impose the conditions

$$\frac{D}{Dt}\left(r - s(\theta,t)\right)\big|_{r=s(\theta,t)} = 0, \quad \left(p - p^{(N)}\right)\Big|_{r=s(\theta,t)} = 0, \tag{30}$$

where the first condition is implemented in an averaged sense, using the average velocities. In terms of the dimensionless variables (15), (30) becomes

$$\overline{U} - \frac{1}{R}\frac{\partial S}{\partial \theta}\overline{V} = \frac{\partial S}{\partial T} = \overline{U}^{(N)} - \frac{1}{R}\frac{\partial S}{\partial \theta}\overline{V}^{(N)}, \quad P - P^{(N)} = 0, \quad R = S(\theta, T),$$

which we expand about $R = A(T)$:

$$\begin{aligned} &\overline{U}\Big|_{R=A} + \frac{\partial \overline{U}}{\partial R}\Big|_{R=A}\zeta - \frac{1}{A}\,\overline{V}\Big|_{R=A}\frac{\partial \zeta}{\partial \theta} + O(\zeta^2) = A'(T) + \frac{\partial \zeta}{\partial T} \\ &= \overline{U}^{(N)}\Big|_{R=A} + \frac{\partial \overline{U}^{(N)}}{\partial R}\Big|_{R=A}\zeta - \frac{1}{A}\,\overline{V}^{(N)}\Big|_{R=A}\frac{\partial \zeta}{\partial \theta} + O(\zeta^2), \\ &P\big|_{R=A} + \frac{\partial P}{\partial R}\Big|_{R=A}\zeta + O(\zeta^2) = P^{(N)}\Big|_{R=A} + \frac{\partial P^{(N)}}{\partial R}\Big|_{R=A}\zeta + O(\zeta^2). \end{aligned} \tag{31}$$

We now insert the perturbation expansions for the average velocities and fluid pressures,

$$\begin{aligned} &\overline{U} = \overline{U}_0 + \overline{U}_1, \quad \overline{V} = \overline{V}_1, \quad P = P_0 + P_1, \\ &\overline{U}^{(N)} = \overline{U}_0^{(N)} + \overline{U}_1^{(N)}, \quad \overline{V}^{(N)} = \overline{V}_1^{(N)} \quad P^{(N)} = P_0^{(N)} + P_1^{(N)}, \end{aligned}$$

into the system of equations in (31), which gives to first order

$$\begin{aligned} &\overline{U}_0\Big|_{R=A} + \overline{U}_1\Big|_{R=A} + \frac{\partial \overline{U}_0}{\partial R}\Big|_{R=A}\zeta = A'(T) + \frac{\partial \zeta}{\partial T} \\ &= \overline{U}_0^{(N)}\Big|_{R=A} + \overline{U}_1^{(N)}\Big|_{R=A} + \frac{\partial \overline{U}_0^{(N)}}{\partial R}\Big|_{R=A}\zeta, \\ &P_0\big|_{R=A} + P_1\big|_{R=A} + \frac{\partial P_0}{\partial R}\Big|_{R=A}\zeta = P_0^{(N)}\Big|_{R=A} + P_1^{(N)}\Big|_{R=A} + \frac{\partial P_0^{(N)}}{\partial R}\Big|_{R=A}\zeta. \end{aligned} \tag{32}$$

From (16) and (27), the depth-averaged radial velocities of the base flow are given by

$$\overline{U}_0(R) = \frac{1}{R} = \overline{U}_0^{(N)}(R), \tag{33}$$

and at $R = A(T)$, we have

$$\overline{U}_0(A) = \overline{U}_0^{(N)}(A) = \frac{1}{A(T)} = A'(T), \qquad \left.\frac{d\overline{U}_0}{dR}\right|_{R=A} = \left.\frac{d\overline{U}_0^{(N)}}{dR}\right|_{R=A} = -A^{-2}. \tag{34}$$

From (34), and the expressions for the zeroth-order pressure gradients in (16) and (27), we see that the zeroth-order equations in (32) are identically satisfied. Using (33), as well as (25) and (28), gives the first order equations

$$-\frac{n}{n+2}A^{1/n-1}\left.\frac{\partial P_1}{\partial R}\right|_{R=A} - A^{-2}\zeta = \frac{\partial \zeta}{\partial T}, \tag{35}$$

$$\frac{n}{n+2}A^{1/n-1}\left.\frac{\partial P_1}{\partial R}\right|_{R=A} = \frac{\mu_{min}(a_0)}{3\mu_N}\left.\frac{\partial P_1^{(N)}}{\partial R}\right|_{R=A}, \tag{36}$$

$$P_1|_{R=A} - P_1^{(N)}\Big|_{R=A} = \left(-\frac{3\mu_N}{\mu_{min}(a_0)}A^{-1} + (n+2)A^{-1/n}\right)\zeta. \tag{37}$$

2.4. Linear stability analysis

We now proceed with a linear stability analysis in which we consider time-dependent perturbations of the form

$$\zeta(\theta, T) = \zeta_k(T)e^{ik\theta}, \tag{38}$$

$$P_1(R,\theta,T) = \phi_k(T)e^{ik\theta}\left(\frac{R}{A(T)}\right)^{kM_k}, \tag{39}$$

$$P_1^{(N)}(R,\theta,T) = \phi_k^{(N)}(T)e^{ik\theta}\left(\frac{R}{A(T)}\right)^{-k}, \tag{40}$$

where $\zeta_k(T)$, $\phi_k(T)$ and $\phi_k^{(N)}(T)$ are functions of T, k =2, 3, ... and

$$M_k = \frac{n-1}{2nk} + \frac{1}{2nk}\sqrt{(n-1)^2 + 4k^2 n}.$$

Note that in the Newtonian case when $n = 1$, $M_k = 1$. The expressions for P_1 and $P_1^{(N)}$ are selected in this way so that equations (26) and (29) are satisfied, and so that P_1 is finite at $R = 0$ and $P_1^{(N)}$ is finite as $R \to \infty$. Substituting (38), (39), and (40) into the boundary conditions (35), (36), and (37), we obtain

$$-\frac{nkM_k}{n+2}A^{1/n-2}\phi_k - A^{-2}\zeta_k = \zeta_k'(T), \tag{41}$$

$$\frac{nM_k}{n+2}A^{1/n-1}\phi_k = -\frac{\mu_{min}(a_0)}{3\mu_N}\phi_k^{(N)}, \tag{42}$$

$$\phi_k - \phi_k^{(N)} = \left(-\frac{3\mu_N}{\mu_{min}(a_0)}A^{-1} + (n+2)A^{-1/n}\right)\zeta_k. \tag{43}$$

Solving (43) for $\phi_k^{(N)}$ and substituting this expression into (42) leads to (see Section 1 in the supplementary Mathematica file Suppl1.nb)

$$\phi_k = \frac{(n+2)A^{-1/n}\left[(n+2)\mu_{min}(a_0)A - 3\mu_N A^{1/n}\right]}{3nM_k\mu_N A^{1/n} + (n+2)\mu_{min}(a_0)A}\zeta_k,$$

which we insert into (41) and simplify further to obtain

$$\zeta_k'(T) = \lambda_k(T)\zeta_k(T),$$

and so

$$\zeta_k(T) = \zeta_k(0)\exp\left[\int_0^T \lambda_k(T)dT\right], \tag{44}$$

where

$$\lambda_k(T) = \frac{1}{A^2}\left[k\frac{\mu_N - \mu_{eff}(a_0)A^{1-1/n}}{\mu_{eff}(a_0)A^{1-1/n}/(nM_k) + \mu_N} - 1\right], \tag{45}$$

and

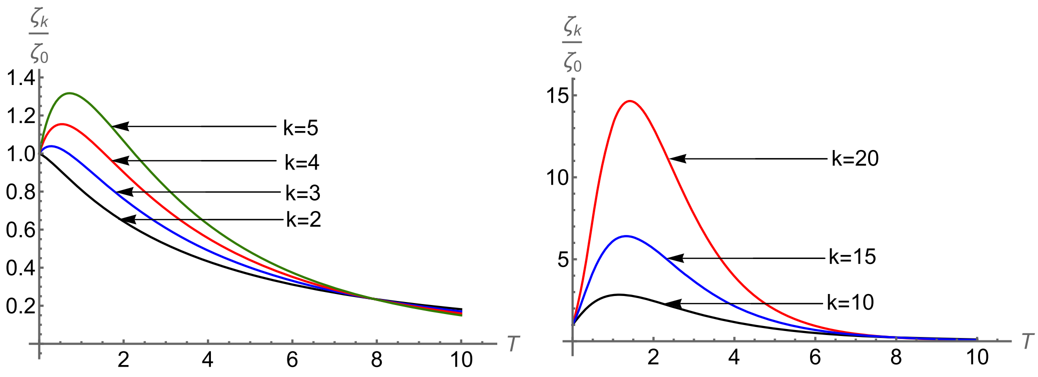

Fig. 2. Plots of ζ_k/ζ_0 against scaled time T for the smallest wave numbers (left) and larger wave numbers (right). For early times $T>0$, each mode grows and reaches a peak amplitude, after which it decreases asymptotically to zero. Larger wave numbers have greater peak amplitudes, but experience quicker decay.

$$\mu_{eff}(a_0) = \frac{n+2}{3}\mu_{min}(a_0), \tag{46}$$

is what we will call the effective viscosity. It is not an average viscosity; due to the implementation of the power-law model, we lose the ability to derive a finite-valued expression for the viscosity at $Z=0$, and so obtaining an average across the gap is not possible. But we can interpret this effective viscosity as an analogue Newtonian viscosity (at least independent of the vertical coordinate Z) by noting that at $T=0$, using (16) and (27), the ratio of the zero-order pressure gradients is

$$\frac{dP_0}{dR}\Big/\frac{dP_0^{(N)}}{dR} = \frac{\mu_{eff}(a_0)}{\mu_N},$$

and from (45), whether this ratio - which is a ratio of two viscosities - is less than or greater than one, plays a fundamental role in the stability of the system in its early stages, when $T\approx 0$ and $A\approx 1$.

We can actually obtain an analytic solution to (44) (see Section 2 in the supplementary Mathematica file Suppl1.nb). In Fig. 2, representative plots of the perturbation amplitudes $\zeta_k(T)$, each scaled by the same initial amplitude ζ_0, against dimensionless time T are shown. Each perturbation (barring that of $k=2$) undergoes an initial increase in amplitude until reaching a peak value, after which the amplitudes decrease, tending asymptotically to zero.

We can study the large time T behaviour by rearranging (45),

$$\lambda_k(T) = \frac{1}{A^2}\left[k\frac{\mu_N A^{1/n-1} - \mu_{eff}(a_0)}{\mu_{eff}(a_0)/(nM_k) + \mu_N A^{1/n-1}} - 1\right],$$

and by noting that $A^{1/n-1}\to 0$ for large T, we obtain

$$\lambda_k(T) = -\frac{1}{A^2}\left(knM_k + 1\right),$$

and because $knM_k = (n-1)/2 + 1/2\sqrt{(n-1)^2+4k^2n}$ is an increasing function of k, we see that the amplitudes decay rapidly with mode number for large T. This observation is supported by the plots in Fig. 2.

2.5. Theoretical estimates

One of the aims of this work is to derive theoretical expressions that can be conveniently compared to experimental results. If we run a series of laboratory experiments for different initial injection radii a_0, keeping all other experimental parameters fixed, as a consequence of the viscosity of the shear-thinning fluid increasing with radial distance from the source, we expect to find a critical radius a_c where for injection radii $a_0 > a_c$ the flow is stable and remains that way for all time, and unstable when $a_0 < a_c$. We might also expect that meeting the condition for instability $a_0 < a_c$ does not necessarily mean that all modes are unstable, and that there might be a critical radius a_k associated with each mode k. For those modes that are unstable initially at $T=0$, from the plots shown in Fig. 2, it seems reasonable to assume that for $T>0$ each mode reaches a peak amplitude with subsequent decay at different times.

In this section, we derive a theoretical expression for the critical radius a_c that governs the initial stability of the interface, as well as the critical radius a_k for each mode k. We also obtain an expression for the dimensionless time T_k^* at which each mode k reaches its maximum amplitude. These theoretical expressions, particularly a_c, provide a very convenient means for comparison between theory and experiment.

2.5.1. Critical injection radii

To determine the condition for which Saffman-Taylor fingers are expected to form initially, we need to examine the sign of λ_k at $T=0$. At $T=0$ we have

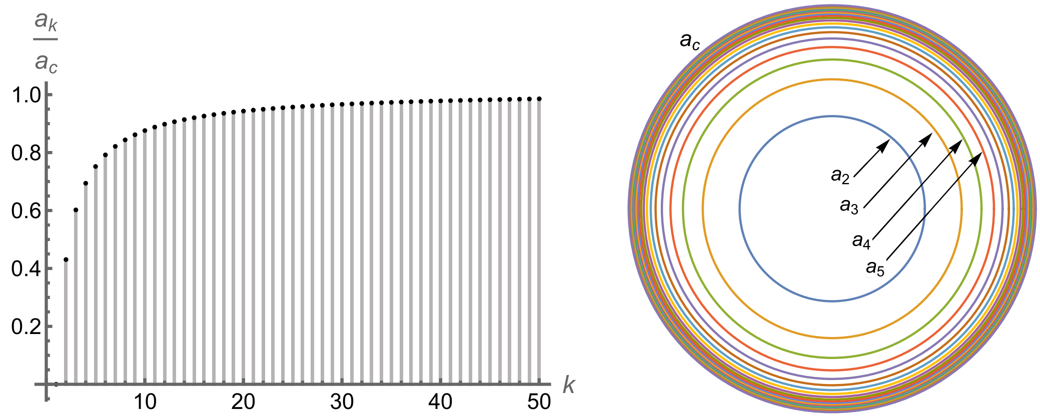

Fig. 3. Plot of a_k/a_c against k (left), and plots of a_k (right). We see that a_k is an increasing function of k with an upper limit of a_c.

$$\lambda_k(0) = k\frac{\mu_N - \mu_{eff}(a_0)}{\mu_{eff}(a_0)/(nM_k) + \mu_N} - 1. \tag{47}$$

From (47), in order for all modes k to be stable, we require $\mu_N < \mu_{eff}(a_0)$. The critical injection radius at which $\mu_N = \mu_{eff}(a_0)$ is given by

$$a_c = \left[\frac{3\mu_N}{m(n+2)}\right]^{n/(n-1)} \frac{(n+2)Q}{8\pi H^2}. \tag{48}$$

Therefore, for injection radii $a_0 > a_c$, any interfacial disturbances will quickly decay resulting in axisymmetric flow. Now, for each mode k to be stable at $T = 0$ we must have $\lambda_k(0) < 0$, which leads to the critical radius

$$a_k = a_c\left[\frac{nM_k(k-1)}{knM_k+1}\right]^{n/(n-1)}, \tag{49}$$

for each mode k.

In Fig. 3 representative plots of the critical radius a_k in (49) scaled by a_c in (48) are shown. We see that $a_{k-1} < a_k < a_{k+1}$ and $a_k \to a_c$ as $k \to \infty$. There is a rather sharp increase observed from $k = 2$ to $k = 10$, followed by a more gradual approach to the limiting value a_c. This theoretical result corresponds to the physical situation where if we begin an experiment with an initial injection radius within the interval $a_k < a_0 < a_{k+1}$, we expect all modes k and smaller to be stable and modes $k+1$ and larger to be initially unstable.

2.5.2. Peak amplitudes and decay of viscous fingers

The representative plots in Fig. 2 suggest that each perturbation amplitude ζ_k increases initially until it reaches a peak value at, say, time T_k^*, and for $T > T_k^*$, the perturbations start to decay. In order to find T_k^* corresponding to the peaks, which signify the start of the decay phase, we need to solve $\lambda_k(T) = 0$:

$$T_k^* = \frac{1}{2}\left[\left(\frac{nM_k(k-1)\mu_N}{(knM_k+1)\mu_{eff}(a_0)}\right)^{2n/(n-1)} - 1\right], \tag{50}$$

which is the dimensionless time at which λ_k ceases its positive contributions to the integral in (44). Alternatively, we can write (50) conveniently as

$$T_k^* = \frac{1}{2}\left[\frac{a_k^2}{a_0^2} - 1\right], \tag{51}$$

which is equivalent to the dimensionless time T it takes $A(T)$ to reach a_k/a_0. Because $a_k < a_{k+1}$ and $a_k \to a_c$, the critical dimensionless time T_k^* is an increasing function of k, i.e. $T_k^* < T_{k+1}^*$ with an upper bound $T_k^* \to T_c^*$ which is found from (51) in the limit as $k \to \infty$:

$$T_c^* = \frac{1}{2}\left[\frac{a_c^2}{a_0^2} - 1\right]. \tag{52}$$

The dimensionless time T_c^* in (52) corresponds to the dimensionless time T it takes $A(T)$ to reach a_c/a_0. For $T > T_c^*$ all k modes will be within the decay phase.

These results are supported by the plots in Fig. 2. There is a delay in the start of the decay phase at $T = T_k^*$ for increasing k. As a result, higher-order modes only begin to decay at later times, and are allowed to increase in amplitude for a longer duration, and so they reach higher maximum amplitudes. However, because T_k^* has an upper limiting value of T_c^*, the delay in the start of the decay phase will not increase without bound. Instead, we expect that for $T > T_c^*$ even the highest order modes will undergo decay.

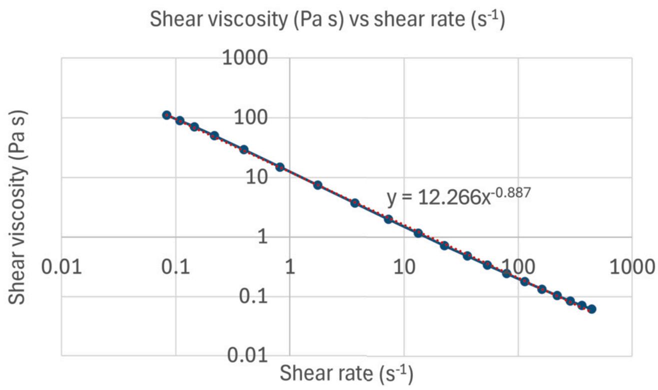

Fig. 4. Shear viscosity (Pa s) versus shear rate (s^{-1}). The data is well-approximated by a power-law model with n and m values given by (53).

Pascal's stability analysis [23], which was applied to the analogous problem of non-Newtonian flow within a porous medium, proved the existence of a series of critical radii corresponding to each mode, which is in broad agreement with our analysis.

3. Comparison with experimental results

The mathematical model developed in this paper is based on simple physical mechanisms described by relatively straightforward mathematics. The aim of this section is to investigate whether this mathematical model is a reasonable representation of the real-life flow behaviour. We approach this task by obtaining values for a_c and a_k, and determining whether these theoretical predictions are reflected in experimental observations. The aim here is not to provide an extensive experimental study; instead, we will see that even a small set of experiments can guide our efforts into developing an improved mathematical model.

In these experiments, Xanthan gum was injected at a constant flux into a small gap between two glass plates, originally occupied by a viscous silicone oil. The Xanthan gum solution was created by mixing 10 g of Xanthan powder with 30 g of vegetable oil, creating a uniform paste, and then combining this paste with 960 g of hot tap water using an electric mixer. The solution was left for 48 hours to cool to room temperature and to allow the lumps and larger bubbles to dissolve.

A rheometer was used to obtain the data for the log-log plot of the shear viscosity μ_{sh} versus shear rate $\frac{\partial u}{\partial z}$ shown in Fig. 4. The model parameters m and n in (6) were then obtained by fitting the data points to

$$\mu_{sh} = 2^{1-1/n} m \left|\frac{\partial u}{\partial z}\right|^{1/n-1}.$$

Using as the approximate shear rate,

$$\frac{\partial u}{\partial z} \sim \frac{Q}{4\pi H^2 r},$$

within the range of experimental parameters (Q = 2 ml s^{-1}, $2H = 0.1$ cm, $r \sim 0.5 - 10$ cm), this solution displayed clear shear-thinning properties with index and consistency constant values

$$n \approx 8.85, \quad m \approx 6.63 \text{ Pa s}^{1/n}. \tag{53}$$

The same Xanthan gum solution was used for each experiment. However, three different silicone oils which varied in viscosity were considered.

The experimental setup consisted of a horizontal square glass plate with each side of length 40 cm with a small hole of radius 0.1 cm at the centre, and a second glass plate separated from the first using plate spacings of 0.1 cm. A syringe pump was used to inject the Xanthan gum into the gap between the plates, through the small hole on the bottom plate. Each experiment started with the top plate removed. A small amount of Xanthan gum was injected onto the lower plate where it spread radially outwards. Silicone oil was added uniformly around the Xanthan gum. The top plate was then gently lowered onto the plate spacings, expelling any residual air, creating an initial disk of Xanthan gum of radius a_0, surrounded entirely by a large disk of silicone oil. The outer radius of the silicone oil disk was chosen to be much larger (about 20 times) than that of the injection radius a_0 so that boundary effects would have negligible impact. The syringe pump was started again at some chosen flux Q, and the Xanthan gum displaced the silicone oil as it spread radially outward.

Photographs of one such experiment are shown in Fig. 5, with the full video in real-time given as Supplementary Material. Xanthan gum, which initially occupied a disk of radius $a_0 = 0.5$ cm at time $t = 0$ s (left), was pumped into a small gap of size $2H = 0.1$ cm between the two plates at a constant flux $Q = 2$ ml s^{-1}, displacing a viscous silicone oil with viscosity $\mu_N = 1$ Pa s. For $t > 0$, disturbances at the interface resembling stubby finger-like protrusions formed, such as the ones shown at $t = 6$ s (middle). The finger-like pattern persisted for a short duration until at later times, $t = 21$ s (right), the amplitudes of the fingers decreased, eventually undergoing complete suppression, returning the flow to its axisymmetric base state.

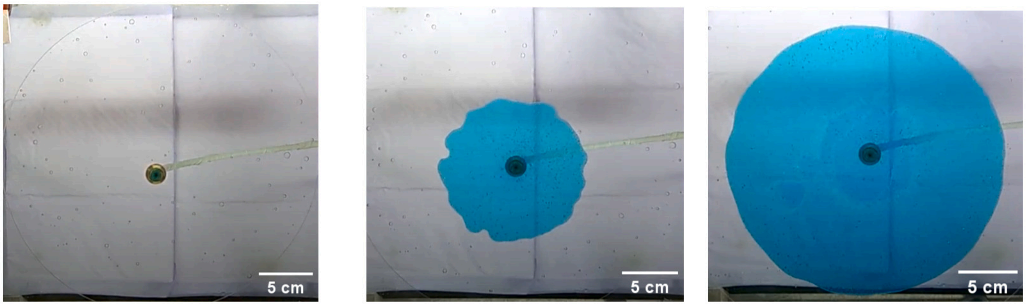

Fig. 5. Photographs of an experiment at different times t where Xanthan gum is injected at a constant flux of $Q = 2$ ml s^{-1} into a small gap of size $2H = 0.1$ cm, displacing a viscous silicone oil of viscosity $\mu_N = 1$ Pa s. At $t = 0$ s (left) the Xanthan gum occupies an approximate disk region of radius $a_0 = 0.5$ cm; at $t = 6$ s (middle) viscous fingers form; and at $t = 21$ s (right) the interfacial disturbances decay. The white line in the bottom right of each image corresponds to a length of 5 cm.

In Tables 1 and 2 photographs of various experiments taken within 10 s from the starting time are shown in the first column, and in the second column, the corresponding experimental parameter values are provided. In each experiment, the gap thickness was kept at $2H = 0.1$ cm. However, parameters such as the initial injection radius a_0, the output flux Q, and the viscosity of the silicone oil μ_N were varied. Theoretical estimates for the effective viscosity at the injection radius $\mu_{eff}(a_0)$, the critical radius a_c, and the critical radius corresponding to the lowest mode a_2 are given in the third column.

In Table 1 the results of four experiments, where Xanthan gum was injected at a constant flux of $Q = 2$ ml s^{-1} displacing a silicone oil of viscosity $\mu_N = 1$ Pa, are shown. The injection radius a_0 was varied from 0.5 cm to 1.8 cm. Interfacial instabilities were observed in all four experiments at early times. These disturbances were significantly larger in the experiments with the smaller injection radii, namely, $a_0 = 0.5$ cm and $a_0 = 0.8$ cm, less pronounced in the experiment with injection radius $a_0 = 1$ cm, and just about noticeable in the experiment with the largest injection radius, $a_0 = 1.8$ cm. Experimental observations at early times also suggested that large wavelength disturbances, which correspond to low-mode numbers, featured prominently in the finger-like patterns in the smaller injection radii experiments, with small wavelength disturbances seen at larger injection radii. The absence of low-mode number disturbances at larger injection radii is captured by the mathematical model, which showed that each mode had a critical radius a_k associated with it, and that this was an increasing function of k. Therefore, as the injection radius a_0 increases through successive values of a_k, a greater number of modes are stabilised.

As encouraging as this result is, two observations in particular cast doubt on the direct applicability of the theoretical model to these experiments. Firstly, although in all four experiments the injection radius was less than the theoretical value of $a_2 = 4$ cm and all modes $k \geq 2$ were predicted to be initially unstable, low-mode number disturbances appeared to feature only in the two smaller injection radii experiments. Secondly, in the experiment with the largest injection radius of $a_0 = 1.8$ cm where the interfacial disturbances were very small in magnitude resulting in an almost-circular interface, it seems somewhat surprising that this injection radius was an order of magnitude smaller than the theoretical prediction for the critical radius $a_c = 9.6$ cm corresponding to stable flow.

These observations were the motivation behind the second set of experiments, the results of which are summarised in Table 2. In the first experiment, the aim was to produce distinct viscous fingers with larger amplitudes. This was achieved by using a much more viscous silicone oil with viscosity $\mu_N = 4.85$ Pa s. The pronounced viscous fingers of Xanthan gum which intruded into the silicone oil showed no signs of suppression as time progressed. To the contrary, the Xanthan gum fingers actually pierced the silicone oil-air interface. Although this is a very interesting result, discussing it is beyond the scope of this work. The aim of the second experiment was to show that we can achieve stable flow at a much smaller injection radius than predicted theoretically. Here silicone oil of viscosity $\mu_N = 0.49$ Pa s was used and the input flux was increased to $Q = 2.6$ ml s^{-1}. With an injection radius of $a_0 = 0.6$ cm, which is an order of magnitude smaller than the theoretical prediction determining stability, $a_c = 5.6$ cm, there were no perceptible interfacial disturbances (at least observed at laboratory flow scales).

The disparity between theory and experiment is significant enough to deduce that it is not likely a result of experimental error. There are a number of factors that are absent from the mathematical model. One such factor includes the effect of the initial perturbation on the stability analysis, which has been investigated in a lifting Hele-Shaw cell [26]. It was shown that the growth rate of the perturbations derived from a linear stability analysis substantially underestimated the onset of instability. By introducing a new stability criterion, which is also based on the initial amplitudes of the perturbations, these authors were able to better predict the onset of instability. This avenue is a worthwhile pursuit for further research, but will require a detailed experimental study, including high-resolution experimental images from which the initial perturbations can be measured. In the current paper, we will explore two other potential improvements - surface tension and wall-slip - for reasons based on experimental observations which will be made apparent in the next section.

4. Improved mathematical model

The simple mathematical model that was developed yielded theoretical predictions for the critical radius a_c that appeared to differ from experimental results by an order of magnitude. However, the model does successfully predict the trends in the fingering patterns: with increasing injection radii, an increasing number of k modes are initially stabilised. So instead of discarding the model

Table 1
Experimental results where Xanthan gum is injected radially at a flux Q into a small gap of size $2H$ where it displaces silicone oil of viscosity μ_N. Each photograph was taken within 10 s from the start of the experiment. Theoretical estimates are given for the effective viscosity of the Xanthan gum $\mu_{eff}(a_0)$ at the injection radius a_0, the critical radius determining stability a_c, and the critical radius corresponding to the lowest mode, a_2.

Experiment	Experimental parameters	Theoretical estimates
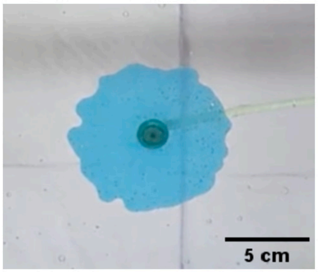	• $a_0 = 0.5$ cm • $2H = 0.1$ cm • $Q = 2$ ml s^{-1} • $\mu_N = 1$ Pa s	• $\mu_{eff}(a_0) = 0.07$ Pa s • $a_c = 9.6$ cm • $a_2 = 4$ cm
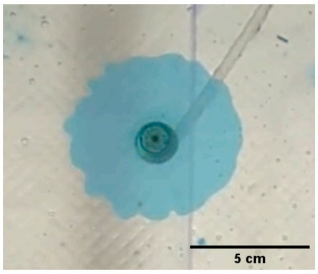	• $a_0 = 0.8$ cm • $2H = 0.1$ cm • $Q = 2$ ml s^{-1} • $\mu_N = 1$ Pa s	• $\mu_{eff}(a_0) = 0.11$ Pa s • $a_c = 9.6$ cm • $a_2 = 4$ cm
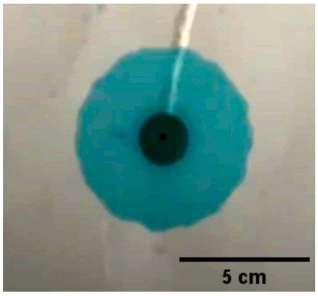	• $a_0 = 1$ cm • $2H = 0.1$ cm • $Q = 2$ ml s^{-1} • $\mu_N = 1$ Pa s	• $\mu_{eff}(a_0) = 0.13$ Pa s • $a_c = 9.6$ cm • $a_2 = 4$ cm
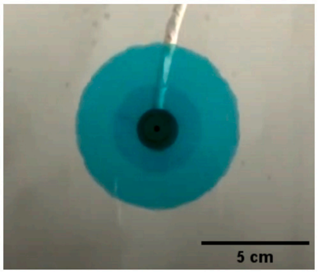	• $a_0 = 1.8$ cm • $2H = 0.1$ cm • $Q = 2$ ml s^{-1} • $\mu_N = 1$ Pa s	• $\mu_{eff}(a_0) = 0.23$ Pa s • $a_c = 9.6$ cm • $a_2 = 4$ cm

completely, in this section we will consider two improvements in isolation, namely, the inclusion of surface tension effects and the reduction of shear due to slip at the walls.

4.1. Role of surface tension

We may expect the role of surface tension at the Xanthan gum-silicone oil interface to play a pivotal role, especially considering the nature of Xanthan gum, which is a water-based solution. We let γ denote the surface tension at the interface between the two fluids, and amend the dynamic boundary condition in (30) to

$$p - p^{(N)} = \gamma \kappa, \quad r = s(\theta, t), \tag{54}$$

where κ is the curvature of the interface. In terms of the dimensionless variables in (15), the dimensionless curvature is

Table 2
Table showing the results of two experiments where Xanthan gum is injected radially at a flux Q into a small gap of size $2H$ where it displaces silicone oil of viscosity μ_N. Theoretical estimates are given for the effective viscosity of the Xanthan gum $\mu_{eff}(a_0)$ at the injection radius a_0, the critical radius determining stability a_c, and the critical radius of the lowest mode, a_2.

Experiment	Experimental parameters	Theoretical estimates
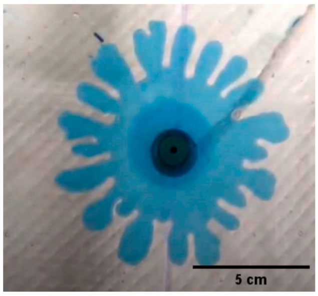	• $a_0 = 1.6$ cm • $2H = 0.1$ cm • $Q = 2$ ml s^{-1} • $\mu_N = 4.85$ Pa s	• $\mu_{eff} = 0.2$ Pa s • $a_c = 57$ cm • $a_2 = 23.7$ cm
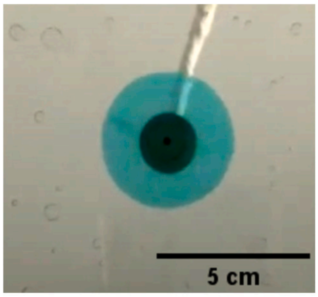	• $a_0 = 0.6$ cm • $2H = 0.1$ cm • $Q = 2.6$ ml s^{-1} • $\mu_N = 0.49$ Pa s	• $\mu_{eff} = 0.07$ Pa s • $a_c = 5.6$ cm • $a_2 = 2.3$ cm

$$a_0\kappa \approx \frac{1}{A} - \frac{1}{A^2}\left(\zeta + \frac{\partial^2\zeta}{\partial\theta^2}\right),$$

and (54) becomes

$$P - P^{(N)} = \frac{4\pi H^3\gamma}{Qa_0\mu_{min}(a_0)}\left[\frac{1}{A} - \frac{1}{A^2}\left(\zeta + \frac{\partial^2\zeta}{\partial\theta^2}\right)\right], \quad R = S(\theta, T).$$

After expanding about $R = A$ as well as inserting the perturbation expansions - much in the same way as in Section 2 - we obtain to first order

$$P_0\big|_{R=A} + P_1\big|_{R=A} + \frac{\partial P_0}{\partial R}\bigg|_{R=A}\zeta = P_0^{(N)}\Big|_{R=A} + P_1^{(N)}\Big|_{R=A} + \frac{\partial P_0^{(N)}}{\partial R}\Bigg|_{R=A}\zeta$$

$$+\frac{4\pi H^3\gamma}{Qa_0\mu_{min}(a_0)}\left[\frac{1}{A} - \frac{1}{A^2}\left(\zeta + \frac{\partial^2\zeta}{\partial\theta^2}\right)\right].$$

To zeroth order we have

$$P_0\big|_{R=A} - P_0^{(N)}\Big|_{R=A} = \frac{4\pi H^3\gamma}{Qa_0\mu_{min}(a_0)}\frac{1}{A},$$

which does not contribute to the stability analysis. The first order equation is

$$P_1\big|_{R=A} + \frac{\partial P_0}{\partial R}\bigg|_{R=A}\zeta = P_1^{(N)}\Big|_{R=A} + \frac{\partial P_0^{(N)}}{\partial R}\Bigg|_{R=A}\zeta - \frac{4\pi H^3\gamma}{Qa_0\mu_{min}(a_0)}\frac{1}{A^2}\left(\zeta + \frac{\partial^2\zeta}{\partial\theta^2}\right), \tag{55}$$

and using (16) and (27), (55) becomes

$$P_1\big|_{R=A} - P_1^{(N)}\Big|_{R=A} = \left(-\frac{3\mu_N}{\mu_{min}(a_0)}A^{-1} + (n+2)A^{-1/n}\right)\zeta$$

$$-\frac{4\pi H^3\gamma}{Qa_0\mu_{min}(a_0)}\frac{1}{A^2}\left(\zeta + \frac{\partial^2\zeta}{\partial\theta^2}\right). \tag{56}$$

Comparing (37) and (56), we see that the effect of surface tension is to introduce an additional term. This additional term contains a ratio of pressures, namely the Laplace pressure, γ/a_0, and the pressure driving the radial flow, $Q\mu_{min}(a_0)/(4\pi H^3)$. The relative importance of these two pressures determines the impact of surface tension.

The next step is to substitute the perturbation expansions (38), (39), and (40) into the boundary conditions. Equations (35) and (36) are unaffected by the inclusion of surface tension. However, (56) results in a more complicated expression for ϕ_k:

$$\phi_k = \frac{(n+2)A^{-1/n}\left[(n+2)\mu_{min}(a_0)A - 3\mu_N A^{1/n}\right]}{3nM_k\mu_N A^{1/n} + (n+2)\mu_{min}(a_0)A}\zeta_k - \frac{4\pi H^3\gamma\left(k^2-1\right)(n+2)}{a_0 QA\left(3nM_k\mu_N A^{1/n} + (n+2)\mu_{min}(a_0)A\right)}\zeta_k. \tag{57}$$

Solving (35), (36) and (57) leads to a modified evolution equation for each mode k (see Section 3 in the supplementary Mathematica file Suppl1.nb) which satisfies equation (44) but the expression for λ_k replaced by

$$\lambda_k(T) = \frac{1}{A^2}\left[k\frac{\mu_N - \mu_{eff}(a_0)A^{1-1/n} - (4\pi H^3\gamma/(3a_0Q))(k^2-1)A^{-1}}{\mu_{eff}(a_0)A^{1-1/n}/(nM_k) + \mu_N} - 1\right]. \tag{58}$$

For the surface tension between Xanthan gum and silicone oil, we will use the approximate value of $\gamma = 0.04$ N/m [27]. Using the experimental parameters provided in Table 1 and running through a range of k values, numerical solutions for a_k, obtained by setting $\lambda_k(0) = 0$ in (58), are found to lie within the range 4 cm - 8.5 cm for integer k values less than 50. For larger values $k \gtrsim 50$, provided the injection radius is finite, i.e. not vanishingly small, surface tension stabilises these modes. Without surface tension, a_k was found to lie within the range 4 cm - 9.6 cm. These results show that surface tension does not have a significant effect on disturbances with mode numbers less than 50. In fact, to get closer to any kind of reasonable agreement between theory and experiment, preliminary calculations suggest that surface tension would need to be more than 10 times its current value. These results indicate that either the effect of surface tension was not adequately captured, or it is not the primary factor causing the mismatch between theory and experiment. The findings in the current study, namely that surface tension would need to be much larger to have an impact on the onset of instability, are mirrored in other studies, see [7] for example.

4.2. Slip at the walls

The effect of wall-slip is likely to play a role in the stability of the fluid-fluid interface as it leads to different viscosity measurements in the shear-thinning fluid [28]. Experimental observations suggest that a small layer of silicone oil is left behind as the Xanthan gum advances, forming a thin lubricating layer separating the Xanthan gum from the cell walls. For example, in the first experiment in Table 1, there appears to be a darker blue disk near to the source surrounded by a lighter blue annular disk suggesting that the Xanthan gum layer is thicker near to the source, and thins with increasing radial distance as a small amount of silicone oil is left behind. Determining the amount of silicone left behind, which will be a function of radial distance from the source and perhaps even evolve with time, is not a trivial exercise. Instead, we consider the extreme case in which the cell boundaries are perfectly lubricated. As a result, the shear-stress becomes negligible and extensional-stress dominates.

In a perfectly-lubricated cell, the viscosity of the shear-thinning fluid is [29]

$$\mu^*(a_0) = \left[\frac{(n+2)a_0}{2H}\right]^{1-1/n}\mu_{min}(a_0). \tag{59}$$

The viscosity in (59) gives theoretical estimates that are significantly greater than those supplied by (46). For example, in the second experiment in Table 1 where $\mu_{eff} = 0.11$, using (59), we obtain a much larger viscosity value of $\mu^* = 1.6$ Pa s. This estimate, obtained using (59), is also larger than the viscosity of the Newtonian fluid μ_N suggesting that if interfacial instabilities do occur, they are not of the Saffman-Taylor type we are investigating. In reality, it is likely that there is significant shear-reduction due to slip at the cell walls, but imposing a perfectly lubricating constraint is too extreme.

It is also entirely possible that wall-slip and surface tension effects cannot be considered in isolation, and a model taking into account both of these effects in tandem would be more suitable, see [30] for example.

5. Conclusions

We derived a mathematical model for the radial displacement of a viscous Newtonian fluid by a shear-thinning fluid within a small gap, using the thin-film equations and appropriate interface conditions. A linear stability analysis, in which sinusoidal perturbations to the fluid-fluid interface were considered, was performed on the system of equations. It was shown that a critical radius a_c exists, such that for initial injection radii $a_0 > a_c$, the interface between the two fluids remained stable. For injection radii $a_0 < a_c$, the flow was initially unstable, and the stability of each mode k was governed by a critical radius a_k, which was an increasing function of k, tending asymptotically to its limiting value of a_c.

The theoretical predictions for a_c and a_k were compared to the results of six laboratory experiments in which Xanthan gum was injected into a silicone oil-filled cell. The theoretical predictions were found to be about an order of magnitude greater than what was observed experimentally. Based on experimental observations, two improvements to the mathematical model were considered: the inclusion of surface tension and the effect of wall-slip. The inclusion of surface tension, although expected to be important as Xanthan gum is a water-based substance that has significant surface tension with oil, did not provide much improvement to the theoretical predictions. Wall-slip, which leads to an increase in the viscosity of the shear-thinning fluid, was only briefly discussed with a more involved treatment reserved for future studies.

There are a number of exciting possibilities for future work:

- Designing an experimental setup that more accurately represents the model developed in the current work. We could consider minimising wall-slip by using a different Newtonian fluid as oils such as silicone oil are prone to leaving thin films on surfaces, or we could use rough or chemically-treated plates instead of smooth ones. With an improved setup, a thorough experimental investigation can be undertaken, with detailed comparisons to predictions from the theoretical model. This would entail obtaining findings such as the initial dominant wave numbers, the time at which the fingers start to undergo suppression, and the time taken for the flow to return to its initial axisymmetric configuration. The effects of experimental parameters such as the gap height, the input flux, the concentration of the Xanthan gum solution, and the initial injection radius would then be investigated.
- We could instead retain the current experimental setup and consider models that account for wall-slip and surface tension in a similar fashion to the work done in [30].
- For any mathematical model, be it the current one in this paper or some improved version of it, the effect of the initial perturbation amplitudes on the stability analysis would be a worthwhile pursuit as such effects have been shown to significantly impact the onset of the fingering instability in a related Hele-Shaw flow problem [26].

Declaration of competing interest

I report no conflicts of interest.

Acknowledgements

I want to express my sincerest gratitude to R Maver, University of Manchester, who will surely be part of the next generation of rising stars, for her invaluable contribution to the laboratory work. I also want to thank M G Worster, University of Cambridge, D P Mason, University of the Witwatersrand, Johannesburg, S G Subramanian and M Quinn, University of Manchester, and T V Ball, University of Warwick for their valuable discussions, comments, and suggestions. Lastly, I want to thank the referees for raising excellent points, prompting changes that have greatly improved this manuscript.

Appendix A. Supplementary material

Supplementary material related to this article can be found online at https://doi.org/10.1016/j.apm.2025.116206.

Data availability

Data will be made available on request.

References

[1] P.G. Saffman, G.I. Taylor, The penetration of a fluid into a porous medium or Hele-Shaw cell containing a more viscous liquid, Proc. R. Soc. Lond. Ser. A, Math. Phys. Sci. 245 (1958) 312–329.
[2] P. Singh, S. Mondal, Role of the process conditions on three-dimensional viscous fingering: impact on enhanced oil recovery and geological storage, Int. J. Multiph. Flow 184 (2025) 105110.
[3] P.G. Saffman, Viscous fingering in Hele-Shaw cells, J. Fluid Mech. 173 (1986) 73–94.
[4] D. Bensimon, L.P. Kadanoff, S. Liang, B.I. Shraiman, C. Tang, Viscous flows in two dimensions, Rev. Mod. Phys. 58 (1986) 977–999.
[5] L. Paterson, Radial fingering in a Hele Shaw cell, J. Fluid Mech. 113 (1981) 513–529.
[6] L. Paterson, Fingering with miscible fluids in a Hele Shaw cell, Phys. Fluids 28 (1) (1985) 26–30.
[7] T.V. Ball, N.J. Balmforth, A.P. Dufresne, Viscoplastic fingers and fractures in a Hele-Shaw cell, J. Non-Newton. Fluid Mech. 289 (2021) 104492.
[8] B. Abedi, L.S. Berghe, B.S. Fonseca, E.C. Rodrigues, R.M. Oliveira, P.R. de Souza Mendes, Influence of wall slip in the radial displacement of a yield strength material in a Hele–Shaw cell, Phys. Fluids 34 (11) (2022) 113102.
[9] A.P. Dufresne, T.V. Ball, N.J. Balmforth, Viscoplastic Saffman–Taylor fingers with and without wall slip, J. Non-Newton. Fluid Mech. 312 (2023) 104970.
[10] A. Lindner, D. Bonn, J. Meunier, Viscous fingering in a shear-thinning fluid, Phys. Fluids 12 (2) (2000) 256–261.
[11] A. Lindner, D. Bonn, E.C. Poiré, M.B. Amar, J. Meunier, Viscous fingering in non-Newtonian fluids, J. Fluid Mech. 469 (2002) 237–256.
[12] P. Singh, R. Lalitha, S. Mondal, Saffman-Taylor instability in a radial Hele-Shaw cell for a shear-dependent rheological fluid, J. Non-Newton. Fluid Mech. 294 (2021) 104579.
[13] J.G. Savins, Non-Newtonian flow through porous media, Ind. Eng. Chem. 61 (10) (1969) 18–47.
[14] L. Kondic, M.J. Shelley, P. Palffy-Muhoray, Non-Newtonian Hele-Shaw flow and the Saffman-Taylor instability, Phys. Rev. Lett. 80 (1998) 1433–1436.
[15] R. Brandão, J. Fontana, J. Miranda, Interfacial pattern formation in confined power-law fluids, Phys. Rev. E 90 (2014) 013013.
[16] P.H. Tordjeman, Saffman-Taylor instability of shear thinning fluids, Phys. Fluids 19 (2007) 118102.
[17] V. Gorodtsov, V. Yentov, Instability of the displacement fronts of non-Newtonian fluids in a Hele-Shaw cell, J. Appl. Math. Mech. 61 (1) (1997) 111–126.
[18] P. Coussot, Saffman–Taylor instability in yield-stress fluids, J. Fluid Mech. 380 (1999) 363–376.
[19] S. Mora, M. Manna, Saffman-Taylor instability for generalized Newtonian fluids, Phys. Rev. E 80 (2009) 016308.
[20] P. Fast, L. Kondic, M.J. Shelley, P. Palffy-Muhoray, Pattern formation in non-Newtonian Hele–Shaw flow, Phys. Fluids 13 (5) (2001) 1191–1212.

[21] S.D.R. Wilson, The Taylor–Saffman problem for a non-Newtonian liquid, J. Fluid Mech. 220 (1990) 413–425.
[22] L. Zhang, Z. Yang, Y. Méheust, I. Neuweiler, R. Hu, Y.-F. Chen, Displacement patterns of a Newtonian fluid by a shear-thinning fluid in a rough fracture, Water Resour. Res. 59 (9) (2023).
[23] H. Pascal, Rheological effects of non-Newtonian behavior of displacing fluids on stability of a moving interface in radial oil displacement mechanism in porous media, Int. J. Eng. Sci. 24 (9) (1986) 1465–1476.
[24] H. Pascal, Stability of non-Newtonian fluid interfaces in a porous medium and its applications in an oil displacement mechanism, J. Colloid Interface Sci. 123 (1) (1988) 14–23.
[25] J.E. Sader, D.Y.C. Chan, B.D. Hughes, Non-Newtonian effects on immiscible viscous fingering in a radial Hele-Shaw cell, Phys. Rev. E 49 (1994) 420–432.
[26] D. Li, Z. Yang, A.A. Pahlavan, R. Zhang, R. Hu, Y.-F. Chen, Stability transition in gap expansion-driven interfacial flow, Phys. Rev. Lett. 133 (2024) 034003.
[27] H. Fox, P. Taylor, W. Zisman, Polyorganosiloxanes...surface active properties, Ind. Eng. Chem. 39 (11) (1947) 1401–1409.
[28] H.A. Barnes, A review of the slip (wall depletion) of polymer solutions, emulsions and particle suspensions in viscometers: its cause, character, and cure, J. Non-Newton. Fluid Mech. 56 (3) (1995) 221–251.
[29] A.J. Hutchinson, M.G. Worster, Fracturing behaviour of a shear-thinning fluid in a lubricated Hele-Shaw cell, J. Fluid Mech. 1003 (2025) A6.
[30] E.O. Dias, J.A. Miranda, Wavelength selection in Hele-Shaw flows: a maximum-amplitude criterion, Phys. Rev. E 88 (2013) 013016.

Dr. Ashleigh Jane Hutchinson is a Lecturer in Applied Mathematics at the University of Manchester, UK. She earned her PhD in 2016 from the University of the Witwatersrand, Johannesburg, South Africa. In 2021, she was awarded a prestigious Newton International Fellowship, which enabled her to conduct research at the University of Cambridge, UK. During this period, she investigated the fracturing behaviour of shear-thinning fluids using a combination of theoretical and experimental approaches. Her current research focuses on problems involving low-Reynolds number flows and non-Newtonian fluids, with a variety of applications in both nature and industry.